

A Mechanism Underpinning the Bioenergetic Metabolism-Regulating Function of Gold Nanocatalysts

Zixin Wang, Alexandre Henriques, Laura Rouvière, Noëlle Callizot, Lin Tan, Michael T. Hotchkin, Rodrigue Rossignol, Mark G. Mortenson, Adam R. Dorfman, Karen S. Ho,* and Hui Wang*

Bioenergetic deficits are known to be significant contributors to neurodegenerative diseases. Nevertheless, identifying safe and effective means to address intracellular bioenergetic deficits remains a significant challenge. This work provides mechanistic insights into the energy metabolism-regulating function of colloidal Au nanocrystals, referred to as CNM-Au8, that are synthesized electrochemically in the absence of surface-capping organic ligands. When neurons are subjected to excitotoxic stressors or toxic peptides, treatment of neurons with CNM-Au8 results in dose-dependent neuronal survival and neurite network preservation across multiple neuronal subtypes. CNM-Au8 efficiently catalyzes the conversion of an energetic cofactor, nicotinamide adenine dinucleotide hydride (NADH), into its oxidized counterpart (NAD⁺), which promotes bioenergy production by regulating the intracellular level of adenosine triphosphate. Detailed kinetic measurements reveal that CNM-Au8-catalyzed NADH oxidation obeys Michaelis–Menten kinetics and exhibits pH-dependent kinetic profiles. Photoexcited charge carriers and photothermal effect, which result from optical excitations and decay of the plasmonic electron oscillations or the interband electronic transitions in CNM-Au8, are further harnessed as unique leverages to modulate reaction kinetics. As exemplified by this work, Au nanocrystals with deliberately tailored structures and surfactant-free clean surfaces hold great promise for developing next-generation therapeutic agents for neurodegenerative diseases.

1. Introduction

The high energy demands of the brain make this organ inherently vulnerable to metabolic perturbations that impact adenosine triphosphate (ATP) synthesis and utilization.^[1] As humans age, metabolic inefficiencies increase in number and degree, putting vulnerable neurons at risk of bioenergetic failure.^[2] Several independent lines of evidence indicate that neurodegenerative diseases, such as Alzheimer's disease (AD), Parkinson's disease (PD), and many others, may result as a manifestation of brain bioenergetic failure associated with aging.^[1,3] Improving cellular bioenergetics may therefore be a promising target for developing novel neurodegenerative disease-modifying therapies.

Nicotinamide adenine dinucleotide (NAD) is a coenzyme that plays crucial roles in energy metabolism in all living cells. NAD exists in two forms: a reduced form, NADH, and an oxidized form, NAD⁺. NADH is used as a fuel for oxidative phosphorylation while NAD⁺ is used for glycolysis to produce ATP. Accordingly, the NADH/NAD⁺ ratio is tightly regulated and


Z. Wang, L. Tan, H. Wang
Department of Chemistry and Biochemistry
University of South Carolina
Columbia, SC 29208, USA
E-mail: wang344@mailbox.sc.edu

A. Henriques, L. Rouvière, N. Callizot
Neuro-Sys
410 D60, Gardanne 13120, France

M. T. Hotchkin, M. G. Mortenson, K. S. Ho
Clene Nanomedicine, Inc.
Salt Lake City, UT 84117, USA
E-mail: karen@clene.com

R. Rossignol
Cellomet
CARF Center
University of Bordeaux
146 rue Léo Saïgnat, Bordeaux 33000, France

M. G. Mortenson, A. R. Dorfman
Clene Nanomedicine, Inc.
North East, MD 21901, USA

 The ORCID identification number(s) for the author(s) of this article can be found under <https://doi.org/10.1002/smll.202304082>

© 2023 The Authors. Small published by Wiley-VCH GmbH. This is an open access article under the terms of the Creative Commons Attribution-NonCommercial License, which permits use, distribution and reproduction in any medium, provided the original work is properly cited and is not used for commercial purposes.

DOI: 10.1002/smll.202304082

controls energy metabolism in the cells. A deficient level of NAD⁺ has been considered a hallmark of bioenergetic deficit as well as a potential therapeutic target for many mitochondrial and neurodegenerative diseases. For example, boosting NAD⁺ levels using genetic or dietary means significantly improves neuronal function, cognition, and survival in AD model organisms.^[4–7] Therapeutic benefits of NAD⁺ have also been documented in models of PD,^[8,9] amyotrophic lateral sclerosis (ALS),^[10,11] and multiple sclerosis (MS).^[12,13] A study of prion disease demonstrated that highly toxic, misfolded prion proteins induced severe, neuron-specific NAD⁺ depletion, followed by decreased intracellular ATP levels.^[14] Replenishment of NAD⁺ to media of prion-treated neuroblastoma cells and intracerebellar injection of NAD⁺ into prion-protein infected mice resulted in significant rescue of neuroblastoma and hippocampal neurons, respectively, from apoptosis.^[14] In contrast, attempts to reduce prion protein levels by activating proteolytic or autophagic pathways had negligible effect on neuronal survival.^[14]

Nanoparticles made of noble metal elements, such as Au, Pt, and Ru, exhibit remarkable catalytic activities toward various biologically relevant chemical reactions, acting as potent, stable enzyme mimetics.^[15–21] Colloidal Au nanoparticles can catalyze the aerobic oxidation of NADH to produce NAD⁺ under physiologic reaction conditions in an aqueous environment,^[22] potentially endowing them with direct therapeutic relevance for a number of neurodegenerative diseases. When harnessing the intrinsic catalytic activity of Au nanoparticles for therapeutic applications, clean nanoparticle surfaces with abundant, fully exposed, and easily accessible active sites but free of any toxic organic capping ligands are highly desired. However, traditional chemical synthesis of colloidal Au nanoparticles relies critically on the use of surface-capping organic ligands, such as amphiphilic surfactant molecules, to guide the nanocrystal growth and stabilize the colloidal suspensions.^[23–25] These organic ligands residing on nanoparticle surfaces, which remain difficult and costly to remove in numerous cases,^[26,27] may not only cause cytotoxicity issues^[28–31] but also lead to compromised catalytic activities.^[27,32–34] CNM-Au8, a federally-registered trademark of Clene Nanomedicine, Inc., is a pharmaceutical grade suspension of Au nanocrystals synthesized using a patented electrochemical method in the absence of any surface-capping organic ligands.^[35,36] CNM-Au8 is the first Au nanocrystal suspension being developed as a therapeutic drug with evidence of remyelinating and neuroprotective activities.^[37] In a preclinical publication,^[37] we showed that orally administered CNM-Au8 penetrated the blood brain barrier and therapeutic levels of CNM-Au8 reached the central nervous system to exert its remyelination activities as well as improve some behavior phenotypes. CNM-Au8 has a clean safety, tolerability, and toxicology profile as demonstrated by multiple, recently completed Phase 2 clinical trials, a first-in-human study, and standard ICH M3 (R2) animal chronic toxicity studies. Phase 2 proof-of-concept studies of CNM-Au8 for the treatment of MS, ALS, and PD are registered in Clinicaltrials.gov (REPAIR-MS: NCT03993171 and VISIONARY-MS: NCT03536559 and NCT04626921; RESCUE-ALS: NCT04098406, HEALEY-ALS Platform trial: NCT04414345, and REPAIR-PD: NCT03815916). The results of Phase 2 brain imaging studies conducted on participants diagnosed with either PD or relapsing MS suggested that orally administered CNM-

Au8 could penetrate the blood brain barrier, consistent with the animal bioavailability results.^[38]

Our previous preclinical studies characterizing CNM-Au8's remyelination activities revealed that CNM-Au8 exhibited intrinsic capabilities to promote NADH oxidation, to induce the differentiation of oligodendrocyte precursor cells into myelinating oligodendrocytes, and to improve remyelination in two independent demyelinating animal models.^[37] These promising preclinical results motivated us to further investigate the neuroprotective properties of CNM-Au8, as detailed below. The neuroprotective function of CNM-Au8 arises from the aerobic oxidation of NADH catalyzed by colloidal Au nanocrystals, which is found to obey the Michaelis–Menten kinetic model. The kinetic results reported in this work indicate that each CNM-Au8 nanocrystal behaves as a NADH dehydrogenase-mimicking nanozyme that regulates the energy homeostasis in living cells. We further demonstrate that photoexcited charge carriers and photothermal transduction resulting from optical excitations and decay of the electronic interband transitions and the localized plasmon resonances in CNM-Au8 nanocrystals can be deliberately harnessed as unique leverages to modulate the kinetic enhancement of the Au-catalyzed NADH oxidation reactions.

2. Results and Discussion

2.1. Neuroprotective Function of CNM-Au8

Neural sensitivity to glutamate excitotoxicity has been considered a significant contributory factor to neurodegeneration.^[39] We used validated *in vitro* neuroprotection assays to assess the neuroprotective efficacies of CNM-Au8 treatment against a range of different primary neural-glial co-cultures. The neuron survival counts, neurite network lengths, and aggregation of transactive response DNA binding protein 43 kDa (TDP-43) in primary motor neurons treated with glutamate and CNM-Au8 were analyzed on the basis of fluorescence microscopy imaging results (representative images are given in Figure S1, Supporting Information). To increase the efficiency of scoring thousands of cell bodies and neurite networks, an automated script made by Neuro-Sys was implemented using the custom module editor (molecular devices). As shown in **Figure 1A,B**, treatment of rat primary motor neurons with CNM-Au8 resulted in dose-responsive, statistically significant improvement of neuron survival and preservation of neurite lengths following glutamate excitotoxicity in comparison to the treatment with the vehicle control (6.5 mM NaHCO₃ without CNM-Au8). We chose riluzole as a benchmark for comparison because this medicine is capable of blocking glutamate neurotransmission^[40] and is one of three Food and Drug Administration-approved drugs for the motor neuron degenerative disease, ALS. CNM-Au8 treatment outperformed riluzole in protecting motor neurons from exogenous glutamate. In addition to primary motor neuron cultures, CNM-Au8 also effectively protected primary hippocampal and cortical neurons from glutamate excitotoxicity in a dose-dependent manner (Figure S2, Supporting Information). Improvements in both neuron survival counts, preservation of synapses, and neurite network lengths were achieved upon CNM-Au8 treatment. These experimental results clearly demonstrated that CNM-Au8 exerted

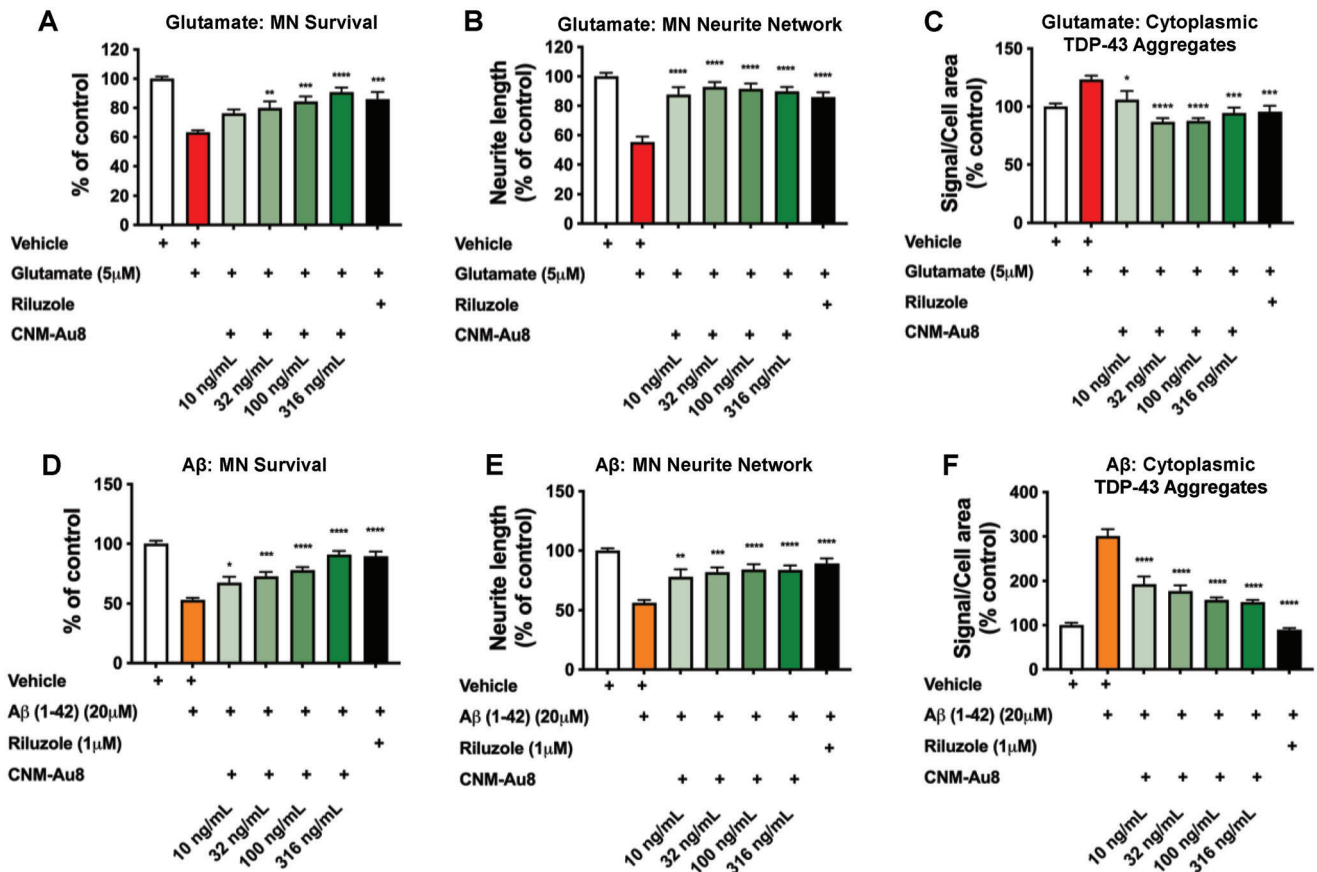


Figure 1. CNM-Au8 treatment increases neuronal survival and protects neurite networks from glutamate challenge and from amyloid-beta oligomer toxicity in vitro. Primary rat E15 spinal motor neurons (MN) were cultured for 11 days then treated with vehicle, CNM-Au8, or riluzole (1 μM, 1 h). Glutamate (5 μM) (Panels A–C) or amyloid-beta (1-42) oligomers (20 μM) (Panels D–F) were added to the cultures to induce neuronal death. Cells were fixed and stained with anti-neurofilament to quantitate neuron survival (A,D) and neurite length (B,E), and co-stained with anti-TDP-43 and DAPI to quantitate cytoplasmic (non-DAPI-overlapping) TDP-43 signal (C,F). Six replicates were performed per condition. Values were expressed as mean ± standard error (SEM). * $p < 0.05$; ** $p < 0.01$; *** $p < 0.001$; **** $p < 0.0001$; treatment versus vehicle, one way ANOVA corrected for multiple comparisons.

neuroprotective activity over the central nervous system cells in a manner agnostic to neuronal subtype.

We have previously shown that CNM-Au8 elevates NAD^+ levels in primary mesencephalic co-cultures that include dopaminergic neurons.^[37] Treatment of primary rat mesencephalic cultures with 6-hydroxydopamine (6-OHDA) causes accumulation of α -syn aggregates, which can be quantified using immunohistochemistry.^[41] We used this assay as a means of investigating the effect of CNM-Au8 on aggregation of α -syn in tyrosine hydroxylase-expressing (TH+) dopaminergic cells. We observed a dose-dependent reduction in the fraction of TH+ neurons containing α -syn aggregates upon treatment with CNM-Au8 (Figure S3, Supporting Information). Similarly, we also studied whether CNM-Au8 affects the mislocalization and aggregation of TDP-43, a protein involved in ALS and also found in a dementia that presents similarly to AD called limbic-predominant age-related TDP-43 encephalopathy.^[42,43] As shown in Figure 1C, CNM-Au8 treatment led to significant reduction of mislocalized, cytoplasmic TDP-43 aggregates in motor neurons exposed to glutamate.

The accumulation of amyloid plaques, which consist primarily of extracellular brain deposits of amyloid-beta ($A\beta$) peptide, is not only a hallmark of AD but also thought to be intimately involved in its pathology. Application of $A\beta$ peptide (1-42 peptide oligomers) to rat primary motor neurons causes motor neuron death, a retraction of neurite processes of the surviving motor neurons, and accumulation of mislocalized TDP-43 in the cytoplasm.^[44] We utilized this assay to investigate the neuroprotective properties of CNM-Au8 when sensitive neurons were exposed to $A\beta$ peptide (see representative microscopy images in Figure S4, Supporting Information). Treatment with CNM-Au8 effectively protected the motor neurons against the effects of $A\beta$ peptide on neuron viability (Figure 1D), neurite process lengths (Figure 1E), and aberrant TDP-43 localization (Figure 1F). Based on these results, we conclude that CNM-Au8 exerts pan-protective effects against a toxic protein of direct relevance to neurodegenerative disease pathophysiology. The results shown in Figure 1 and Figure S3, Supporting Information, also indicated that CNM-Au8 exerted its neuroprotective effects in a manner independent of the initial insult. CNM-Au8

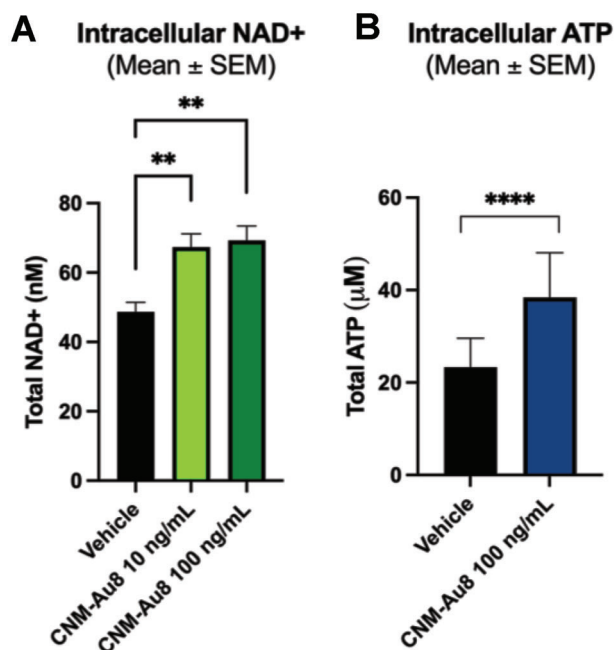


Figure 2. CNM-Au8 treatment increases intracellular levels of NAD⁺ and ATP. A) Primary rat E15 mesencephalic co-cultures were grown for 4 days and then treated with vehicle or CNM-Au8 for 48 h. Cells were then lysed and intracellular levels of NAD⁺ were quantitated. Six replicates were performed per condition. B) Human glial M03.13 cells were cultured with vehicle or CNM-Au8 for 72 h. Total intracellular ATP was quantitated in cell lysates by luciferase assay. Three replicates were performed per condition. Values were expressed as mean ± standard error (SEM). * $p < 0.05$; ** $p < 0.01$; *** $p < 0.001$; **** $p < 0.0001$; treatment versus vehicle, two-tailed t -test.

could effectively protect neurons against different types of toxins primarily by enhancing neuronal fitness and survival rather than selectively blocking a specific toxin from intoxicating the cells.

The neuroprotective function of CNM-Au8 is believed to be intimately tied to Au-catalyzed conversion of NADH to NAD⁺ in the intracellular environment, which could form a critical part of the mechanism underpinning the therapeutic effects of CNM-Au8.^[37] Because of the role of NAD⁺ in bioenergetic metabolism regulation, an increase in the intracellular NAD⁺ pool promoted by CNM-Au8 would be expected to result in higher intracellular levels of ATP, which was confirmed by the results shown in **Figure 2**. The results of recently completed Phase 2 clinical studies revealed that oral dosing of CNM-Au8 effectively modulated the levels of brain energy metabolites, such as NAD⁺, NADH, and ATP, in favorable manners, consistent with a target engagement and potential therapeutic effect in the treated patients.^[38] CNM-Au8 nanocrystals essentially served as an efficient nanocatalyst that kinetically boosted the aerobic oxidation of NADH to produce NAD⁺, effectively regulating the bioenergetic metabolism and protecting neurons from degeneration. Here we studied the detailed kinetic features of the CNM-Au8-catalyzed NADH oxidation reactions, which enabled us to gain mechanistic insights into the origin of the bioenergetic metabolism-regulating function of Au nanocatalysts.

2.2. Michaelis–Menten Kinetics of CNM-Au8-Catalyzed NADH Oxidation

As schematically illustrated in **Figure 3A**, the complete redox reaction catalyzed by CNM-Au8 involved the participation of NADH, H⁺, and the molecular O₂ dissolved in water, with NAD⁺ and H₂O serving as the products of the oxidation and reduction half reactions, respectively. The CNM-Au8 nanocrystals exhibited a quasi-spherical morphology and a multiply twinned crystalline structure (**Figure 3B**), with particle diameters narrowly distributed around 11.3 nm (**Figure 3C**). Although synthesized in a unique reaction environment free of any organic capping ligands, the CNM-Au8 nanocrystals exhibited excellent colloidal stability in aqueous reaction environments over a broad range of pHs because their surfaces were protected by physisorbed bicarbonate anions. Within the pH range of 3–9, the zeta-potentials of colloidal CNM-Au8 remained negative and became more negative as pH increased, while the hydrodynamic sizes of CNM-Au8 appeared almost pH-independent (**Figure S5**, Supporting Information). The crystallographic and surface structures of CNM-Au8 were characterized in greater detail in a previously published work.^[37] Here we further characterized the surface atomic coordinations and measured the specific surface areas of CNM-Au8 nanocrystals using a cyclic voltammetry-based electrochemical oxide stripping assay.^[45–50] During the anodic potential sweep, the Au surface atoms were oxidized to form an oxide adlayer on the nanocrystal surfaces as the applied potential exceeded certain threshold values. Because the undercoordinated surface atoms at the surface defects, domain boundaries, and locally curved surface sites were oxidized more easily than their counterparts on the atomically flat terraces, the oxidation potential downshifted as the surface atomic coordination number decreased.^[47–50] As shown in **Figure 3D**, two characteristic oxidation peaks during the anodic potential sweep were centered at 1.00 and 1.18 V versus saturated calomel electrode (SCE), signifying the electrochemical oxidation of undercoordinated Au surface atoms. In contrast, the close-packed surface atoms on the terraces or crystallographic facets, typically the {111} and {100} facets, were oxidized in a more positive potential range above ≈1.3 V (vs SCE). The cyclic voltammetry results clearly revealed that the surfaces of CNM-Au8 had a high abundance of undercoordinated surface atoms. During the cathodic potential sweep, a sharp reduction peak emerged within the potential window from ≈1.00 to ≈0.85 V (vs SCE), which was the electrochemical signature of the oxide adlayer stripping. Assuming a specific charge of 450 µC cm⁻²,^[51] the mass-specific electrochemically active surface area (ECSA) of CNM-Au8 nanocrystals was estimated to be ≈23.1 ± 1.1 m² g⁻¹, in fairly good agreement with the theoretically predicted mass-specific surface area of an Au nanosphere with a diameter of 11.3 nm (27.6 m² g⁻¹).

We used UV–vis absorption spectroscopy as an in situ spectroscopic tool to monitor the progress of Au-catalyzed NADH oxidation in real time. NADH has two characteristic absorption peaks centered at the wavelengths of 340 and 260 nm, respectively. The peak at 340 nm is the spectral signature of the $n-\pi^*$ transition of the dihydronicotinamide unit, while the absorption peak at 260 nm corresponds to the $\pi-\pi^*$ transition of the adenine ring.^[52] The molar absorption coefficients of NADH at 340 and 260 nm are 6220 and 14100 M⁻¹cm⁻¹, respectively.^[53] The

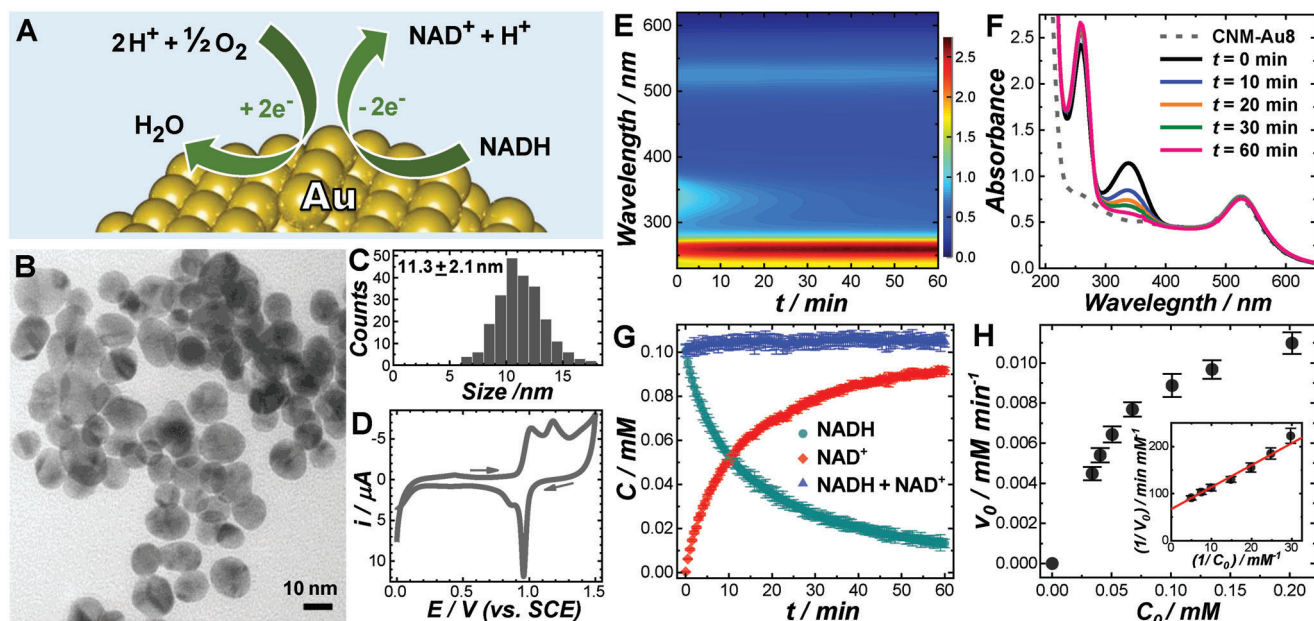


Figure 3. A) Schematic illustration of Au-catalyzed NADH oxidation. B) Transmission electron microscopy (TEM) image and C) particle size distribution of CNM-Au8. D) Cyclic voltammogram collected from a CNM-Au8-loaded working electrode in an N_2 -purged aqueous electrolyte containing 0.5 M H_2SO_4 at room temperature. The potential sweep rate was 5.0 mV s^{-1} and the arrows showed the direction of potential sweep. E) Temporal evolution of UV-vis absorption spectra and F) snapshot UV-vis spectra at various reaction times during the CNM-Au8-catalyzed NADH oxidation at room temperature in a neutral environment (pH of 7). The mass concentration of Au catalysts was 37.7 mg L^{-1} and the initial concentration of NADH was 0.10 mM . G) Temporal evolution of NADH concentration, NAD^+ concentration, and the total concentration of NADH and NAD^+ during the CNM-Au8-catalyzed NADH oxidation reaction at a pH of 7. H) Relationship between the initial reaction velocity and the initial concentrations of NADH. The Lineweaver–Burk plot is shown in the inset. The curve fitting result is shown as a solid red line in the inset of panel H.

oxidized product, NAD^+ , also strongly absorbs light at 260 nm, with a molar absorption coefficient ($16900\text{ M}^{-1}\text{cm}^{-1}$) even higher than that of NADH. Figure 3E shows the temporal evolution of UV-vis absorption spectra during CNM-Au8-catalyzed aerobic oxidation of NADH in a neutral aqueous medium (pH of 7) at room temperature ($22\text{ }^\circ\text{C}$). Several snapshot spectra captured at various reaction times are highlighted in Figure 3F. The initial molarity of NADH was 0.10 mM and the mass concentration of CNM-Au8 nanocatalysts was kept at 37.7 mg L^{-1} (0.191 mM Au atoms). The light extinction peak centered at $\approx 528\text{ nm}$, which was spectral feature of the localized plasmon resonances sustained by CNM-Au8 nanocrystals, remained essentially unshifted with negligible intensity changes (Figure 3E,F), indicating that colloidal Au nanocatalysts remained well-dispersed without forming aggregates during the reaction. As the catalytic reaction proceeded, the absorption intensity at 340 nm progressively decreased while the absorption peak at 260 nm became increasingly more intense. Based on the Lambert–Beer’s law and the molar absorption coefficients of NADH and NAD^+ , we were able to further convert the experimentally measured absorbance to the molar concentrations of NADH and NAD^+ . As shown in Figure 3G, the decrease in NADH concentration, $C(\text{NADH})$, was accompanied by the increase in NAD^+ concentration, $C(\text{NAD}^+)$, with the sum of $C(\text{NADH}) + C(\text{NAD}^+)$ kept almost unchanged throughout the entire reaction process, indicating that neither long-lived intermediates nor side products were observed in the UV-vis absorption spectroscopic results. One of the key parameters for kinetic analysis was the initial reaction velocity, v_0 , whose value could be

extracted by fitting the temporal evolution of $C(\text{NADH})$ at the initial stage of the reactions with a linear function. When keeping the mass concentration of the CNM-Au8 nanocatalysts fixed at 37.7 mg L^{-1} and the pH fixed at 7, the relationship between v_0 and the initial NADH concentration, C_0 , could be well-described by the steady-state Michaelis–Menten kinetic model (Figure 3H), indicating that CNM-Au8 essentially functioned as a nanozyme (enzyme-mimicking nanocatalyst) while NADH served as a substrate to the nanozyme. A linear relationship between the reciprocal of v_0 and the reciprocal of C_0 was clearly observed (inset of Figure 3H), which allowed us to obtain the values of the Michaelis constant, K_m , and the maximal velocity, v_{max} , by fitting the experimental results with the Lineweaver–Burk equation

$$\frac{1}{v_0} = \frac{K_m}{v_{\text{max}}} \times \frac{1}{C_0} + \frac{1}{v_{\text{max}}} \quad (1)$$

At a fixed mass concentration of CNM-Au8 and initial concentration of NADH, the reaction rate increased significantly as the reaction medium became more acidic (Figure 4A) because the catalytic NADH oxidation reactions involved protons and the affinity of reactants to the Au nanozyme surfaces was pH-dependent. Although the reaction rates changed significantly upon variation of pH, the kinetic features of the reactions could always be well-described using the Michaelis–Menten model over a broad range of pHs from 3 to 9 (Figure 4B,C). As the pH progressively increased, the values of v_{max} extracted from least-squares curve fitting decreased monotonically until

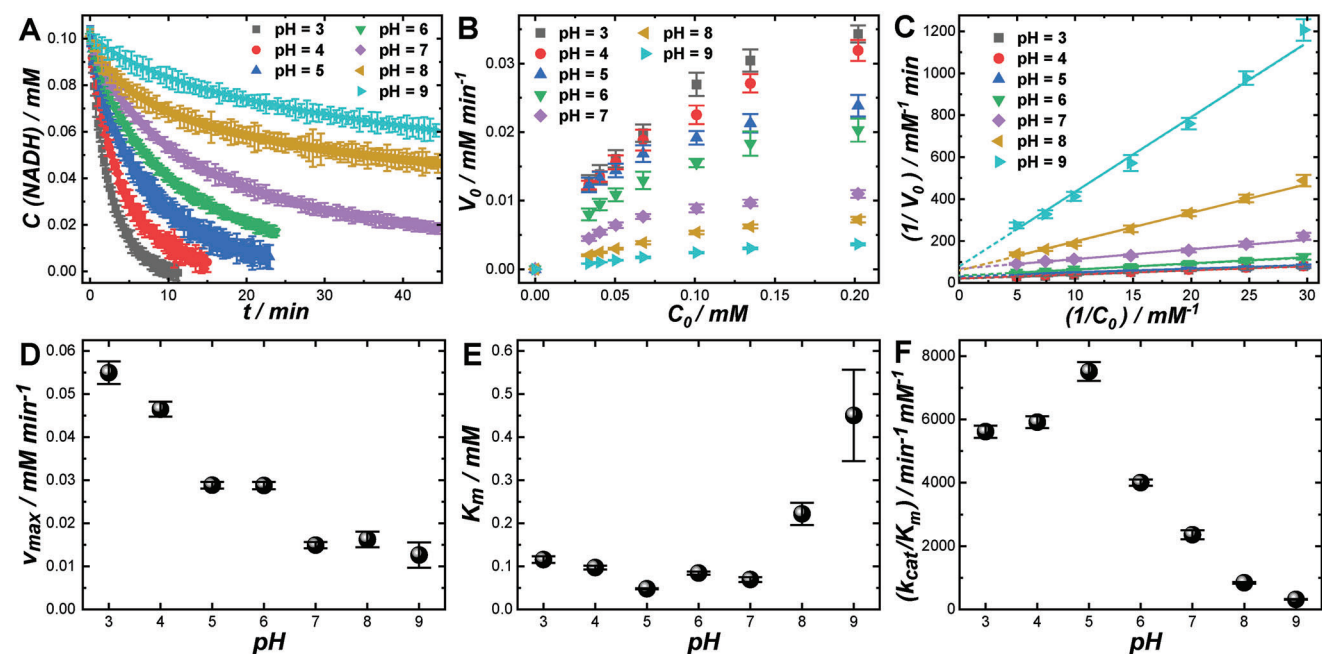


Figure 4. A) Temporal evolutions of NADH concentration during CNM-Au8-catalyzed NADH oxidation reactions at various pHs at room temperature. The mass concentration of Au catalysts was 37.7 mg L^{-1} and the initial concentration of NADH was 0.10 mM . B) Relationships between v_0 and C_0 at various pHs for the reactions occurring at room temperature. C) Lineweaver–Burk plots at various pHs. pH-dependence of D) v_{max} , E) K_{m} , and F) $k_{\text{cat}}/K_{\text{m}}$.

reaching a plateaued value around $0.015 \text{ mM min}^{-1}$ at pHs above 7 (Figure 4D). The values of K_{m} remained close to 0.1 mM in acidic environments at pHs below 7, whereas a significant increase of K_{m} was observed upon further elevation of pH in the alkaline environment (Figure 4E). The pH-dependence of v_{max} and K_{m} shown in Figure 4D,E indicated that increase of pH values not only led to decrease of the turnover number, k_{cat} , which was defined as v_{max} normalized against the nanozyme concentration, C_{nanozyme} , but also weakened the interactions between the NADH substrate and the Au nanozyme. We further calculated the catalytic efficiency, $k_{\text{cat}}/K_{\text{m}}$, at various pHs using the following equation

$$\frac{k_{\text{cat}}}{K_{\text{m}}} = \frac{v_{\text{max}}}{K_{\text{m}} C_{\text{nanozyme}}} = \frac{v_{\text{max}}}{K_{\text{m}}} \times \frac{\pi d^3 \rho N_{\text{A}}}{6 C_{\text{Au}}} \quad (2)$$

in which d is the average diameter of CNM-Au8 nanocrystals (11.3 nm), ρ is the mass density of Au (19.3 g cm^{-3}), N_{A} is the Avogadro's number ($6.02 \times 10^{23} \text{ mol}^{-1}$), and C_{Au} is the mass concentration of Au in the reactant mixtures (37.7 mg L^{-1}). CNM-Au8 appeared catalytically more efficient in acidic environments than in alkaline environments, reaching the maximal catalytic efficiencies around pH of 5 (Figure 4F). While there is typically one active site on each natural enzyme molecule, each CNM-Au8 nanocrystal may have multiple active sites on its surface. To assess the intrinsic catalytic efficiency at a single active site, the calculated values of $k_{\text{cat}}/K_{\text{m}}$ need to be further normalized against the number of active sites on each CNM-Au8 particle, which remains unknown at this point.

The pH-dependent catalytic behaviors of CNM-Au8 were further studied through electrochemical measurements. Figure S6,

Supporting Information, shows the CV curves collected from glassy carbon electrodes (GCEs) and GCEs loaded with CNM-Au8 in electrolytes containing 1 mM NADH at various pHs. In acidic electrolytes, both the onset potential, E_{onset} , and the peak potential, E_{p} , for the NADH oxidation were shifted negatively when CNM-Au8 was loaded onto the working electrodes, suggesting that CNM-Au8 was capable of catalyzing the NADH oxidation. Because of the involvement of protons, E_{p} became more positive as pH increased. In acidic electrolytes, E_{p} exhibited lower values on CNM-Au8-loaded GCEs than on GCEs, whereas such differences in E_{p} values diminished in alkaline environments at pHs above 7. The results of the electrochemical measurements further confirmed that the nanocrystals in CNM-Au8 were catalytically more active toward NADH oxidation in acidic environments than in alkaline environments. Regardless of pH, the electrochemical oxidation of NADH on GCEs and CNM-Au8 exhibited diffusion-controlled kinetic features, as the anodic peak current, i_{p} , appeared proportional to the square-root of the potential sweep rate, $v^{1/2}$, in the linear sweep voltammetry results (Figure S7, Supporting Information).

The CNM-Au8-catalyzed NADH oxidation reactions could be kinetically modulated not only by adjusting pH but also by varying the concentration of dissolved molecular O_2 in the aqueous medium (Figure S8, Supporting Information). When purging the catalyst-reactants mixtures with O_2 , the reactions became kinetically faster than those occurring under ambient air. In contrast, purging the catalyst-reactants mixtures with N_2 led to slower reaction rates due to decreased concentrations of dissolved O_2 . These observations strongly indicated that both NADH and O_2 were substrate molecules to the Au nanozymes. An enzymatic reaction involving two different substrate molecules may occur through

either a ping-pong mechanism, in which the reaction proceeds with the release of one product prior to the association of the other substrate, or a sequential mechanism, which requires the co-adsorption of both substrates to the enzyme before the product molecules are generated and released from the enzyme. These two fundamentally distinct mechanisms could be distinguished from each other by inspecting the Lineweaver–Burk plots at various concentrations of dissolved O_2 . For a ping-pong mechanism, such a plot will yield a series of straight lines that are parallel to each other because the slopes are independent of O_2 concentrations. However, the Lineweaver–Burk plots for the sequential mechanism yield a family of unparallel straight lines that intersect to the negative side of the $(1/v_0)$ axis. The kinetic results shown in Figure S8, Supporting Information, revealed that the CNM-Au8-catalyzed NADH oxidation involved the formation of a nanozyme-NADH- O_2 ternary complex, following the sequential mechanism rather than the ping-pong mechanism.

The overall catalytic activities of CNM-Au8 were intimately tied to the atomic level surface structures of the nanocrystals. We observed a gradual decay in the catalytic activities of CNM-Au8 over multiple cycles of reactions at a pH of 3 (Figure S9, Supporting Information). In each reaction cycle, we monitored the temporal evolution of NADH at a fixed mass concentration of CNM-Au8 of 37.7 mg L^{-1} and initial NADH concentration of 0.10 mM . After NADH was completely converted into NAD^+ , a new cycle of catalytic reaction was initiated upon introduction of additional NADH, which brought the NADH concentration back to 0.10 mM . The activity decay over multiple reaction cycles was a ubiquitous phenomenon observed over a broad range of pHs (Figure S10, Supporting Information), which was found to be related to the atomic level surface restructuring of CNM-Au8 nanocrystals during the catalytic reactions. Although the CNM-Au8 nanocrystals recycled after five cycles of reactions at pH of 3 exhibited no observable changes in particle sizes or morphologies in the TEM images in comparison to the as-synthesized CNM-Au8, the results of CV-based surface oxide stripping measurements showed that the fraction of undercoordinated Au surface atoms decreased considerably after five reaction cycles, while the mass-specific ECSA was well-preserved (Figure S11, Supporting Information). The above-mentioned observations strongly suggested that the undercoordinated surface atoms served as the primary active sites for the catalytic NADH oxidation reactions. Due to the absence of organic capping ligands on the CNM-Au8 nanocrystal surfaces, these active sites were easily accessible to reactant molecules. In Figure S12, Supporting Information, we further compared the catalytic performances of CNM-Au8 to those of Au quasi-spherical nanoparticles (QSNPs, $11.1 \pm 0.4 \text{ nm}$ in diameter) and surface-roughened nanoparticles (SRNPs, $152 \pm 4.8 \text{ nm}$ in diameter), whose surfaces were coated with a bilayer of capping surfactants, cetyltrimethylammonium chloride (CTAC). Although CNM-Au8 and the CTAC-capped Au QSNPs exhibited similar particle sizes and morphologies, the surface capping of CTAC led to remarkably decreased catalytic activity. As shown in detail in our previous publications,^[54–57] Au SRNPs had high abundance of undercoordinated surface atoms, well-mimicking the locally curved surface structures of sub-10 nm nanoparticles. However, due to presence of surface-capping CTAC molecules and significantly larger particle sizes, the Au SRNPs exhibited a mass-specific catalytic activity drasti-

cally lower than that of CNM-Au8. Therefore, highly abundant undercoordinated surface atoms and organic ligand-free clean surfaces were both key contributory factors leading to the remarkable catalytic activities of CNM-Au8 toward NADH oxidation.

When CNM-Au8 is used for biocatalysis *in vivo*, its intrinsic catalytic activity may be influenced by protein coronas formed on its surfaces. We conducted some preliminary *in vitro* studies to investigate how the formation of protein coronas on CNM-Au8 surfaces influenced the catalytic activity of the materials. We incubated human serum albumin (HSA), which constitutes more than 50% of serum proteins, at concentrations ranging from 0 to $10 \mu\text{g mL}^{-1}$, with a fixed concentration of CNM-Au8 ($5 \mu\text{g mL}^{-1}$) to form the coronas. The colloidal stability of CNM-Au8 was well-preserved, and no nanoparticle aggregation was observed at HSA concentrations up to $10 \mu\text{g mL}^{-1}$ (Figure S13, Supporting Information). We then carried out the standard UV–vis absorption spectroscopy-based NADH catalysis assay to evaluate the activities of CNM-Au8 nanocrystals with various surface coverages of HSA. We observed that higher coverage of HSA on CNM-Au8 surfaces led to lower apparent catalytic activity (Figure S14, Supporting Information). The effects of surface-capping by protein coronas in living systems, however, are expected to be significantly more complicated than what we observed in the *in vitro* studies because when the nanocrystals traverse inter- and intracellular milieus, they interact with a huge library of different biomolecules in drastically varying local environments, which causes the corona structures and compositions to change dynamically. The results of our Phase 2 clinical studies^[58] provide the best evidence to date indicating that CNM-Au8 remains catalytically effective in the human brain.

We further compared the *in vitro* neuroprotective efficacy (capability to improve motor neuron survival in response to glutamate challenge) and catalytic activity (oxidation of NADH at room temperature and at a pH of 7) of CNM-Au8 to those of three commercial Au nanoparticle samples, including laser-ablated, monodisperse 20 nm Au nanoparticles (IMRA, Cat. No. AU20-5-50), tannic acid-capped, monodisperse 10 nm Au nanoparticles (Sigma-Aldrich, Cat. No. 752 584), and citrate-capped, monodisperse 10 nm Au nanoparticles (MK Nano, Cat. No. MKN-AU-S010). The TEM images of these commercial Au nanoparticles are shown in Figure S15, Supporting Information. While both laser-ablated Au nanoparticles (LA-Au) and citrate-capped Au nanoparticles (CC-Au) did not significantly improve or decrease neuron survival compared to glutamate alone, tannic acid-capped Au nanoparticles (TC-Au) treatment decreased neuron survival (Figure S16, Supporting Information). The catalytic activities decreased in the order of CNM-Au8 > TC-Au > CC-Au > LA-Au (Figure S17, Supporting Information). Both CNM-Au8 nanocrystals and LA-Au particles had surfaces that were free from organic stabilizing agents. However, laser ablation may favor the formation of thermodynamically stable surfaces, giving rise to atomic-level surface structures remarkably different from those of the electrochemically synthesized CNM-Au8 nanocrystals. Therefore, LA-Au exhibited substantially lower neuroprotective and catalytic efficacies in comparison to CNM-Au8. Although both TC-Au and CC-Au had similar particle sizes as CNM-Au8, the surface capping by tannic acid and citrate led to diminished neuroprotective efficacy and significantly decreased catalytic activities.

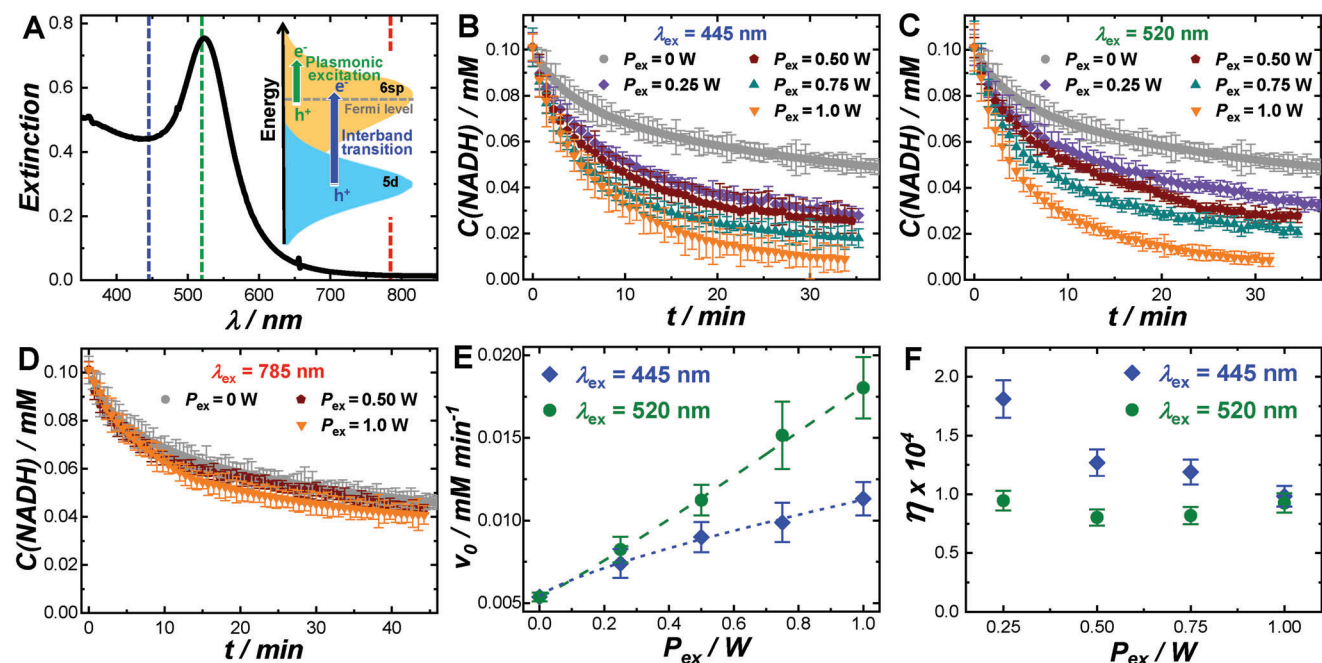


Figure 5. A) Light extinction spectrum of colloidal CNM-Au8. The vertical dash lines indicate the wavelengths of the excitation lasers used in this work. The inset schematically illustrates the photoexcitation of hot electrons and holes upon excitations of the interband transitions and the intraband plasmon resonances. Temporal evolutions of NADH concentration during CNM-Au8-catalyzed NADH oxidation reactions under photo-illumination at λ_{ex} s of B) 445, C) 520, and D) 785 nm and various P_{ex} s. The reactions occurred at a pH of 8 under isothermal conditions with temperature controlled at 22 ± 0.5 °C. The mass concentration of Au catalysts was 37.7 mg L^{-1} and the initial concentration of NADH was 0.10 mM. P_{ex} -dependence of E) v_0 and F) η at λ_{ex} s of 445 and 520 nm. The experimentally measured P_{ex} -dependence of v_0 was fitted with Equation (3) and the curve fitting results were shown as dash curves in panel E.

2.3. Kinetic Enhancements under Light Illumination

Au nanoparticles exhibit intriguing optical properties that are dominated by the collective oscillation of free electrons, also known as plasmons. The photoexcitation and decay of plasmons give rise to a cascade of photophysical processes, including enhancements of local fields on nanoparticle surfaces, generation of non-equilibrium hot charge carriers, and photothermal transduction, all of which may play crucial roles in driving or enhancing photocatalytic transformations of molecular adsorbates on the metal nanocrystal surfaces.^[59–72] Because the particle size of CNM-Au8 (below 20 nm) is well within the quasi-static limit, CNM-Au8 nanocrystals behave as strong visible light-absorbers upon resonant excitation of their plasmons with negligibly small contribution of scattering to the overall light extinction. Although limited local-field enhancements are achievable on the surfaces of small Au nanoparticles, CNM-Au8 is expected to be more efficient in producing hot charge carriers than their counterparts with larger particle sizes, which is beneficial for hot carrier-driven plasmonic photocatalysis. Au nanoparticles also strongly absorb light on the higher-energy side of their plasmon resonances due to interband electronic transitions from the valence band (5d) to the conduction band (6sp).^[73–75] When the excitation photon energy exceeds the interband energy threshold of Au (energy above ≈ 2.4 eV, wavelength below ≈ 516 nm), hot electrons and holes can also be generated upon excitation of d-to-sp interband transitions. While the interband hot carriers are typically considered to have lower kinetic energies as those of the intraband

plasmonic hot carriers, they can also be effectively harnessed to drive photocatalytic reactions, achieving even higher photocatalytic efficiencies than those of plasmon-driven reactions in certain cases.^[73,74] Internal decay of the plasmonic and interband hot carriers within a metallic nanoparticle results in local heating of the nanoparticle itself, followed by heat dissipation to its surrounding medium. Such photothermal effects can also be harnessed to accelerate chemical transformations of molecular adsorbates on the nanoparticle photocatalyst surfaces.^[72,76] In this work, we used both the hot carriers and photothermal heating resulting from interband and plasmonic excitations as unique leverages to kinetically maneuver the CNM-Au8-catalyzed NADH oxidation reactions at a remarkable level of precision.

We chose continuous wave (CW) lasers with emission lines at 445 and 520 nm as the light sources to excite the interband transitions and plasmon resonances of colloidal CNM-Au8, respectively, while a CW excitation laser with an emission line at 785 nm was used for the control experiments under off-resonance conditions (Figure 5A). The mass concentration of CNM-Au8 catalysts was fixed at 37.7 mg L^{-1} with a total volume of the catalyst-reactant mixtures kept at 2.0 mL. The excitation lasers were collimated with a $4 \text{ mm} \times 4 \text{ mm}$, square-shaped illumination cross-section and incident vertically from the top surface into the catalyst-reactants mixtures in a $1.0 \text{ cm} \times 1.0 \text{ cm} \times 4.5 \text{ cm}$ quartz cuvette. The catalyst-reactants mixtures were kept under constant magnetic stir (800 rpm) to facilitate heat dissipation such that thermal equilibria were rapidly established between the nanoparticles and the bulk solution. To

eliminate the temperature elevation caused by photothermal transduction, a circulating water bath was used to maintain an isothermal reaction condition by controlling the bulk solution-phase temperature at 22 ± 0.5 °C. As shown in Figure 5B,C, the CNM-Au8-catalyzed reactions were significantly accelerated under illuminations by the 445 and 520 nm lasers, and increasing the illumination power led to increased reaction rates. However, at an excitation wavelength (λ_{ex}) of 785 nm, the reaction rates under photo-illumination and in dark were observed to be almost the same (Figure 5D) because the excitation photons were off-resonant with the plasmons and energetically insufficient for the excitations of the interband transitions. We fitted the experimentally measured P_{ex} -dependence of reaction rates at the initial stage of the reactions with following power function (Figure 5E)

$$v_{0,\text{light}} = \alpha \left(\frac{P_{\text{ex}}}{1 \text{ W}} \right)^n + v_{0,\text{dark}} \quad (3)$$

in which $v_{0,\text{light}}$ and $v_{0,\text{dark}}$ refer to the initial reaction velocities under photo-illumination and in dark, respectively. α is a fractional coefficient and n is an exponent. $v_{0,\text{light}}$ was observed to increase almost linearly with P_{ex} when the plasmon resonances were excited at λ_{ex} of 520 nm, and the n value obtained from least squares curve fitting (1.09 ± 0.04) was very close to 1. In contrast, a sublinear P_{ex} -dependence of reaction rates was clearly observed with an n value of 0.75 ± 0.05 at λ_{ex} of 445 nm when the interband transitions were optically excited. Such sublinear P_{ex} -dependence of reaction rates is also a common kinetic feature of exciton-driven photocatalysis on semiconductors.^[64,77]

We further compared the apparent quantum efficiencies, η , for the reaction kinetic enhancements under the intraband plasmonic ($\lambda_{\text{ex}} = 520$ nm) and interband ($\lambda_{\text{ex}} = 445$ nm) excitations (Figure 5F). Here, η was defined as the ratio between the number of electrons harnessed for the reactions and the number of photons absorbed by the CNM-Au8 particles over a reaction time of 360 s. η was calculated using the following equation

$$\eta = \frac{2hcVN_{\text{A}} (C_{360\text{s,dark}} - C_{360\text{s,light}})}{360 \text{ s} \times P_{\text{ex}} \lambda_{\text{ex}} \left[1 - 10^{-E(\lambda_{\text{ex}})} \right]} \quad (4)$$

where h is the Planck's constant (6.626×10^{-34} m² kg s⁻¹), c is the speed of light (3.0×10^8 m s⁻¹), V is the total volume of the catalyst-reactants mixtures (2.0×10^{-3} L), and N_{A} is Avogadro's number (6.022×10^{23} mol⁻¹). $C_{360\text{s,light}}$ and $C_{360\text{s,dark}}$ are the concentrations of NADH at a reaction time of 360 s under light illumination and in dark, respectively. $E(\lambda_{\text{ex}})$ is the optical extinction at the excitation wavelength, λ_{ex} , with an optical path length of 2 cm. When P_{ex} was varied within the sub-mW range, η decreased as P_{ex} increased at λ_{ex} of 445 nm, whereas η appeared almost independent of P_{ex} at λ_{ex} of 520 nm. The linear power-dependence of reaction rates and power-independent quantum efficiencies have been considered as kinetic signatures of plasmonic hot carrier-driven reactions under isothermal conditions.^[64,77,78] For photocatalytic reactions driven by interband excitations, the thermalization or recombination of the interband hot carriers becomes prevalent in the high-power regime, leading to sublinear power dependence of reaction rates and decreased quantum efficiencies at higher excitation powers.^[73]

In addition to the plasmonic and interband hot carriers, the photothermal heating effects could also be harnessed to kinetically boost the CNM-Au8-catalyzed NADH oxidation reactions. We systematically studied the kinetics of the reactions taking place in ambient air under continuous laser illuminations without using the temperature-controlled circulating water bath. We consistently observed that the reactions became faster at λ_{ex} s of both 445 and 520 nm when the circulating water bath was removed (Figure 6A,B and Figure S18, Supporting Information). Because the thermal conductivity of air was substantially lower than that of water, the dissipation of the heat generated from photothermal transduction became significantly slower, which resulted in elevation of the temperatures in the catalyst-reactants system. We monitored the temperature evolutions of colloidal CNM-Au8 (37.7 mg L⁻¹) and pure water under continuous laser illuminations at various P_{ex} s until the temperature reached plateaued values, T_{eq} , at the thermal equilibria, followed by natural cooling of the samples down to room temperature in dark (Figure 6C,D). Considerably higher temperatures were reached at the thermal equilibria in colloidal CNM-Au8 than in water because of photothermal transduction resulting from the interband and plasmonic excitations of the colloidal Au nanoparticles. The temperature elevation caused by photothermal transduction of CNM-Au8 (T_{eq} of colloidal suspensions of CNM-Au8 subtracted by T_{eq} of pure water, $T_{\text{eq,H}_2\text{O}}$) was found to be linearly dependent on P_{ex} for both the interband and plasmonic excitations (Figure 6E).

We calculated the photothermal transduction efficiency, ϕ , based on a widely used thermophysical model.^[79–81] The values of the thermal equilibrium time constant, τ_{s} , were obtained by fitting the temporal evolution of $-\ln(\theta)$ during natural cooling in dark with a linear function (Figure S19, Supporting Information)

$$-\ln(\theta) = \frac{t}{\tau_{\text{s}}} \quad (5)$$

where θ refers to the driving force toward thermal equilibrium, which is defined as

$$\theta \equiv \frac{T - T_0}{T_{\text{eq}} - T_0} \quad (6)$$

Here, T_0 is the ambient temperature (22 °C in our case). At the thermal equilibrium, the heat generation and dissipation occur at the same rate, and ϕ can be calculated using the following equation

$$\phi = \frac{m_{\text{H}_2\text{O}} C_{\text{p,H}_2\text{O}} \left(\frac{1}{\tau_{\text{s}}} \Delta T_{\text{eq}} - \frac{1}{\tau_{\text{s,H}_2\text{O}}} \Delta T_{\text{eq,H}_2\text{O}} \right)}{P_{\text{ex}} \left[1 - 10^{-E(\lambda_{\text{ex}})} \right]} \times 100\% \quad (7)$$

in which $m_{\text{H}_2\text{O}}$ and $C_{\text{p,H}_2\text{O}}$ are the mass and constant-pressure heat capacity of water ($m_{\text{H}_2\text{O}} = 2.0$ g and $C_{\text{p,H}_2\text{O}} = 4.184$ J K⁻¹ g⁻¹), respectively. ΔT_{eq} and $\Delta T_{\text{eq,H}_2\text{O}}$ represent temperature elevation of colloidal suspensions of CNM-Au8 and pure water, respectively, at the thermal equilibrium. $\tau_{\text{s,H}_2\text{O}}$ refers to the τ_{s} of water in the absence of CNM-Au8 nanocrystals. As shown in Figure 6F, ϕ values of plasmonic excitations at λ_{ex} of 520 nm were slightly higher (within 10%) than those of interband

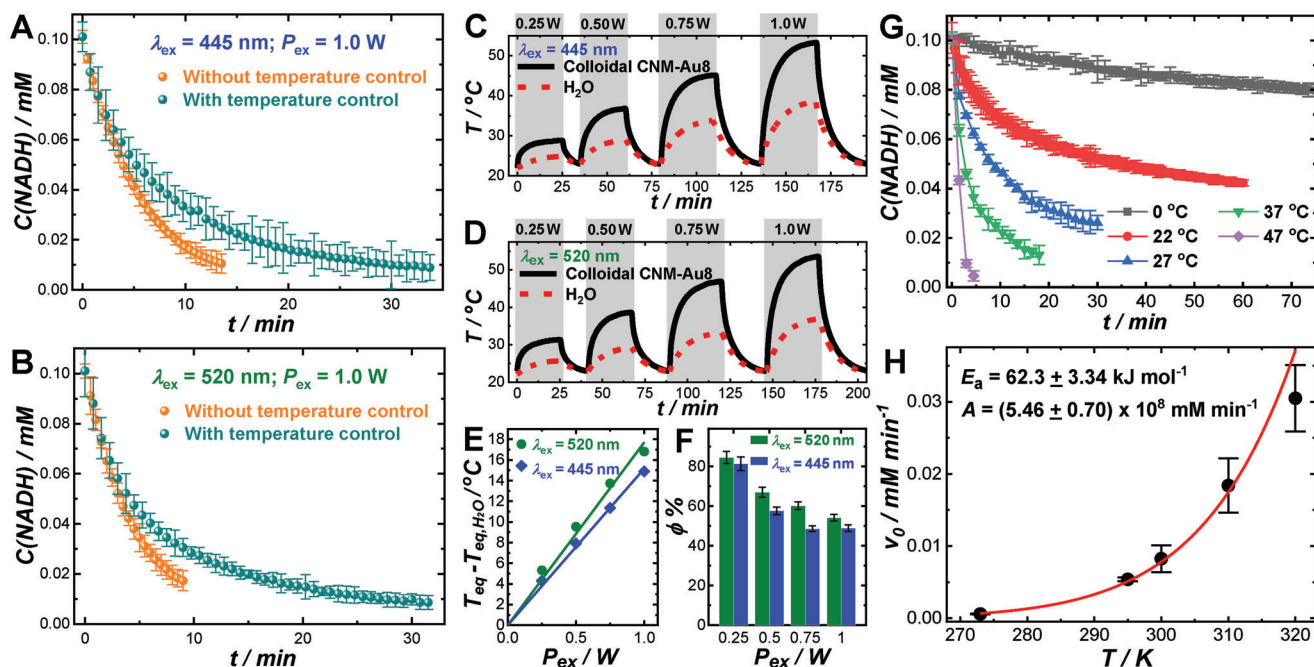


Figure 6. Temporal evolutions of NADH concentration during CNM-Au8-catalyzed NADH oxidation reactions under photo-illumination at a P_{ex} of 1.0 W and λ_{ex} s of A) 445 nm and B) 520 nm with and without temperature control. Temporal evolutions of the bulk temperatures of colloidal CNM-Au8 (37.7 mg L^{-1}) and water under multiple cycles of photo-illumination by the C) 445 and D) 520 nm lasers at various P_{ex} s and natural cooling in dark under ambient air. P_{ex} -dependence of E) $T_{\text{eq}} - T_{\text{eq,H}_2\text{O}}$ and F) ϕ . G) Temporal evolutions of NADH concentration during CNM-Au8-catalyzed NADH oxidation reactions in dark at various reaction temperatures. H) Relationship between v_0 and reaction temperature at a pH of 8. The experimental results were fitted with the Arrhenius equation. In all reactions, the mass concentration of Au catalysts was kept at 37.7 mg L^{-1} and the initial concentration of NADH was 0.10 mM .

excitations at λ_{ex} of 445 nm at identical P_{ex} s, with higher ϕ values observed at lower P_{ex} s at each λ_{ex} . Comparison of the reaction rates under photo-illuminations with and without temperature control, together with the photothermal results, strongly indicated that photothermal heating kinetically boosted the CNM-Au8-catalyzed NADH oxidation reactions.

To further confirm the effects of temperature elevation on the kinetic enhancements, we studied the kinetics of dark reactions without laser illumination at various constant temperatures by immersing the catalyst-reactants mixtures in a temperature-controlled water bath. As shown in Figure 6G, increase of the reaction temperature led to significant acceleration of the reactions at the pH of 8. At a fixed initial concentration of NADH and a fixed catalyst mass concentration, v_0 becomes directly proportional to the rate constant of the rate-limiting step, which is the k_{cat} of a Michaelis–Menten enzymatic reaction. Therefore, the relationship between v_0 and the temperature, T , could be well-described by the Arrhenius equation

$$v_0 = A \exp\left(-\frac{E_a}{RT}\right) \quad (8)$$

in which E_a is the apparent activation energy of the rate-limiting step, R is the molar gas constant ($8.314 \text{ J mol}^{-1} \text{ K}^{-1}$), and A is a pre-exponential factor. By fitting the experimental results with the Arrhenius equation, the value of E_a at pH of 8 was determined to be $62.3 \pm 3.34 \text{ kJ mol}^{-1}$. At pH of 5, the Arrhenius relationship between v_0 and T was still held (Figure S20, Supporting Informa-

tion). Switching the pH from 8 to 5 resulted in a decrease of E_a by $\approx 12.1 \text{ kJ mol}^{-1}$, fully in line with the pH-dependent catalytic behaviors of CNM-Au8 observed in this work.

3. Conclusions

We have found that a pharmaceutical grade suspension of electrochemically synthesized Au nanocrystals, referred to as CNM-Au8, may function as a NADH dehydrogenase-mimicking nanozyme that regulates energy metabolism and thereby effectively protects the central nervous system cells in a manner agnostic to the neuron types. The neuroprotective function of CNM-Au8 arises from Au-catalyzed aerobic oxidation of NADH, which obeys the Michaelis–Menten kinetic model. The high abundance of under-coordinated surface atoms and the organic ligand-free clean surfaces of CNM-Au8 nanocrystals have been found to be two critical factors leading to the remarkable catalytic activities of CNM-Au8 toward NADH oxidation. To the best of our knowledge, CNM-Au8 is so far the only Au nanocrystal with clean, faceted surfaces in development as a catalytically active therapeutic agent for neurodegenerative disease and thus, represents a candidate for first-in-class pharmacotherapy. Other Au nanoparticles with bioactive molecular ligands covalently bound to their surfaces have also been utilized to treat various diseases; however, they differ fundamentally from CNM-Au8 because the execution of their therapeutic functions relies critically on their surface ligands.^[82–84] The insights gained from this work provide important guiding principles for rational design of noble metal-based nanozymes with

energy metabolism-regulating and neuroprotective functions. We have further demonstrated that photoexcited charge carriers and photothermal transduction, which are derived from optical excitations of either the plasmonic electron oscillations or the interband electronic transitions in CNM-Au8, can be judiciously harnessed to further enhance the reaction kinetics under visible light illumination in a highly controllable manner. By deliberately tailoring the sizes and shapes of Au nanocrystals, it becomes possible to tune the plasmon resonance frequencies over a broad spectral range across the visible spectral region into the near-infrared water window, in which tissues and blood become transparent. Using the deep-penetrating near-infrared light to fine-regulate the bioenergetic metabolism in living cells opens up a new avenue for further improving the efficacy of Au nanoparticle-based therapeutic agents for neurodegenerative diseases.

4. Experimental Section

Materials Syntheses and Characterizations: The chemicals and reagents were used as received without further purification (see a detailed list in the Supporting Information). Ultrapure water with a resistivity of 18.2 M Ω (Barnstead EasyPure II 7138) was used for all experiments. CNM-Au8 was synthesized using a previously published and patented electrochemical method.^[35,37] The CNM-Au8 nanocrystals were characterized by TEM, light extinction spectroscopy, cyclic voltammetry, and electrophoretic and dynamic light scattering measurements, as detailed in the Supporting Information. CTAC-capped Au QSNPs^[85] and SRNPs^[54–57] were synthesized following previously published protocols (see details in the Supporting Information).

Kinetic Measurements of Catalytic Reactions: The reaction progress of NADH oxidation under various conditions was tracked in real time based on the temporal evolution of NADH concentrations using an Agilent 8453 UV–vis–NIR spectrophotometer. The catalytic reactions were carried out in a 1 cm \times 1 cm \times 4.5 cm quartz cuvette containing various initial concentrations of NADH in citrate buffers at various pHs. The total volume of the catalyst-reactants mixtures was kept at 2.0 mL. The mass concentration of CNM-Au8 was 37.7 mg L⁻¹. The reactions occurred under an isothermal condition using a temperature-controlled water bath. CW lasers purchased from Lasever Inc. (Ningbo, Zhejiang, China) with the tunable power output in the range of 0–3.0 W and emission wavelengths at 445 (model no. LSR445SD), 520 (model no. LSR520CPD), and 785 nm (model no. LSR785NL) were used as the light sources for the photo-illuminated reactions. The excitation lasers were collimated with a 4 mm \times 4 mm, square-shaped illumination cross-section and incident vertically from the top surface into 2 mL of catalyst-reactants mixtures. The catalyst-reactants mixtures were kept under constant magnetic stir (800 rpm) to facilitate heat dissipation. For photo-illuminated reactions under isothermal conditions, a circulating water bath was used to control the bulk solution-phase temperature at 22 \pm 0.5 $^{\circ}$ C. The temperature evolution during photo-illumination and natural cooling was monitored using a digital thermocouple (Therma Waterproof Thermometer for Type K Thermocouples, Priggen Special Electronic).

Statistical Analysis of the Results of In Vitro Neuroprotection Assays: Protocols for the in vitro neuroprotection assays are described in detail in the Supporting Information. For in vitro neuroprotection assays, the measurements under each condition were performed in six replicates. Values were expressed as mean \pm standard error (SEM). Statistical analyses were performed by one-way ANOVA followed by Dunnett's or Fisher's least significant difference test to correct for multiple comparisons. $p < 0.05$ (designated, “*”) or as specified in Figure legend) was considered significant. Excel (Microsoft v.16.73) and Prism 10.0 (GraphPad v.10.0.0) were used for statistical analyses and chart generation. Photoshop 2023 (Adobe v.24.5.0) was used to assemble micrographs and images.

Supporting Information

Supporting Information is available from the Wiley Online Library or from the author.

Acknowledgements

K.S.H. and H.W. contributed equally to this work. Clene Nanomedicine, Inc. funded this research. The authors thank Random42 and Bjorn Pendleton (Pendleton Creative, LLC) for the Table of Contents artwork. This work used a Hitachi HT7800 transmission electron microscope in the Electron Microscopy Center at University of South Carolina, which was purchased using funds provided by a NSF EPSCoR RII Track-I Award (OIA-1655740). The authors also thank Prof. Qian Wang of University of South Carolina for using his instrument for the measurements of zeta-potentials and hydrodynamic sizes as well as Melanie Gallagher, Gabrielle Goodnow, Michelle Kang, and Misty McClothlin of Clene Nanomedicine for the assessment of the colloidal stability of CNM-Au8 incubated with HSA.

Conflict of Interest

Z.W., L.T., and H.W. declare no conflict of interest. K.S.H., M.T.H., M.G.M., and A.R.D. are full time employees of Clene Nanomedicine, Inc. and own shares in the company. A.H., L.R., and N.C. are full-time employees of Neuro-Sys, a private contract research organization. R.R. is the co-founding CEO and CSO of CELLOMET, a private contract research organization.

Data Availability Statement

The data that support the findings of this study are available from the corresponding author upon reasonable request.

Keywords

bioenergy metabolism, catalytic therapeutics, gold nanocrystals, nanozymes, neurodegenerative diseases, neuroprotection

Received: May 15, 2023

Revised: August 17, 2023

Published online:

- [1] S. Camandola, M. P. Mattson, *EMBO J.* **2017**, *36*, 1474.
- [2] H. Fu, J. Hardy, K. E. Duff, *Nat. Neurosci.* **2018**, *21*, 1350.
- [3] M. Mamelak, *Neurosci. Biobehav. Rev.* **2017**, *75*, 297.
- [4] Y. J. Hou, S. Lautrup, S. Cordonnier, Y. Wang, D. L. Croteau, E. Zavala, Y. Q. Zhang, K. Moritoh, J. F. O'Connell, B. A. Baptiste, T. V. Stevensner, M. P. Mattson, V. A. Bohr, *Proc. Natl. Acad. Sci. U. S. A.* **2018**, *115*, E1876.
- [5] A. N. Long, K. Owens, A. E. Schlappal, T. Kristian, P. S. Fishman, R. A. Schuh, *BMC Neurol.* **2015**, *15*, 19.
- [6] B. Gong, Y. Pan, P. Vempati, W. Zhao, L. Knable, L. Ho, J. Wang, M. Sastre, K. Ono, A. A. Sauve, G. M. Pasinetti, *Neurobiol. Aging.* **2013**, *34*, 1581.
- [7] X. Xie, Y. Gao, M. Zeng, Y. Wang, T.-F. Wei, Y.-B. Lu, W.-P. Zhang, *Metab. Brain Dis.* **2019**, *34*, 353.
- [8] D. C. Schöndorf, D. Ivanyuk, P. Baden, A. Sanchez-Martinez, S. De Cicco, C. Yu, I. Giunta, L. K. Schwarz, G. Di Napoli, V. Panagiotakopoulou, S. Nestel, M. Keatinge, J. Pruszkak, O. Bandmann, B. Heimrich, T. Gasser, A. J. Whitworth, M. Deleidi, *Cell Rep.* **2018**, *23*, 2976.

- [9] H. Jia, X. Li, H. Gao, Z. Feng, X. Li, L. Zhao, X. Jia, H. Zhang, J. Liu, *J. Neurosci. Res.* **2008**, *86*, 2083.
- [10] B. A. Harlan, M. Pehar, D. R. Sharma, G. Beeson, C. C. Beeson, M. R. Vargas, *J. Biol. Chem.* **2016**, *291*, 10836.
- [11] E. Blacher, S. Bashiardes, H. Shapiro, D. Rothschild, U. Mor, M. Dori-Bachash, C. Kleimeyer, C. Moresi, Y. Harnik, M. Zur, M. Zabari, R. B.-Z. Briq, D. Kviatcovsky, N. Zmora, Y. Cohen, N. Bar, I. Levi, N. Amar, T. Mehlman, A. Brandis, I. Biton, Y. Kuperman, M. Tsoory, L. Alfahel, A. Harmelin, M. Schwartz, A. Israelson, L. Arike, M. E. V. Johansson, G. C. Hansson, et al., *Nature* **2019**, *572*, 474.
- [12] V. K. C. Nimmagadda, T. K. Makar, K. Chandrasekaran, A. R. Sagi, J. Ray, J. W. Russell, C. T. Bever, *J. Neuroimmunol.* **2017**, *304*, 29.
- [13] W. Penberthy, I. Tsunoda, *Curr. Pharm. Des.* **2009**, *15*, 64.
- [14] M. Zhou, G. Ottenberg, G. F. Sferazza, C. Hubbs, M. Fallahi, G. Rumbaugh, A. F. Brantley, C. I. Lasmézas, *Brain* **2015**, *138*, 992.
- [15] H. Ye, Z. Xi, K. Magloire, X. Xia, *ChemNanoMat* **2019**, *5*, 860.
- [16] S. B. He, L. Yang, M. T. Lin, P. Balasubramanian, H. P. Peng, Y. Kuang, H. H. Deng, W. Chen, *Biomed. Mater.* **2021**, *16*, 032001.
- [17] G. Xu, X. Du, W. Wang, Y. Qu, X. Liu, M. Zhao, W. Li, Y.-Q. Li, *Small* **2022**, *18*, 2204131.
- [18] Y. Huang, J. Ren, X. Qu, *Chem. Rev.* **2019**, *119*, 4357.
- [19] Y. Lin, J. Ren, X. Qu, *Acc. Chem. Res.* **2014**, *47*, 1097.
- [20] H. Wei, E. Wang, *Chem. Soc. Rev.* **2013**, *42*, 6060.
- [21] J. Wu, X. Wang, Q. Wang, Z. Lou, S. Li, Y. Zhu, L. Qin, H. Wei, *Chem. Soc. Rev.* **2019**, *48*, 1004.
- [22] X. Huang, I. H. El-Sayed, X. Yi, M. A. El-Sayed, *J. Photochem. Photobiol. B* **2005**, *81*, 76.
- [23] C. D. e. M. Donegá, *Chem. Soc. Rev.* **2011**, *40*, 1512.
- [24] S. Mourdikoudis, L. M. Liz-Marzán, *Chem. Mater.* **2013**, *25*, 1465.
- [25] S. E. Lohse, C. J. Murphy, *Chem. Mater.* **2013**, *25*, 1250.
- [26] J.-W. Park, J. S. Shumaker-Parry, *ACS Nano* **2015**, *9*, 1665.
- [27] J. A. Lopez-Sanchez, N. Dimitratos, C. Hammond, G. L. Brett, L. Kesavan, S. White, P. Miedziak, R. Tiruvalam, R. L. Jenkins, A. F. Carley, D. Knight, C. J. Kiely, G. J. Hutchings, *Nat. Chem.* **2011**, *3*, 551.
- [28] J. S. Bozich, S. E. Lohse, M. D. Torelli, C. J. Murphy, R. J. Hamers, R. D. Klaper, *Environ. Sci.: Nano* **2014**, *1*, 260.
- [29] C. Carnovale, G. Bryant, R. Shukla, V. Bansal, *ACS Omega* **2019**, *4*, 242.
- [30] O. Choi, T. E. Clevenger, B. Deng, R. Y. Surampalli, L. Ross Jr, Z. Hu, *Water Res.* **2009**, *43*, 1879.
- [31] Z. V. Feng, I. L. Gunsolus, T. A. Qiu, K. R. Hurley, L. H. Nyberg, H. Frew, K. P. Johnson, A. M. Vartanian, L. M. Jacob, S. E. Lohse, M. D. Torelli, R. J. Hamers, C. J. Murphy, C. L. Haynes, *Chem. Sci.* **2015**, *6*, 5186.
- [32] M. Cargnello, C. Chen, B. T. Diroll, V. V. T. Doan-Nguyen, R. J. Gorte, C. B. Murray, *J. Am. Chem. Soc.* **2015**, *137*, 6906.
- [33] R. D. Neal, R. A. Hughes, P. Sapkota, S. Ptasinaka, S. Neretina, *ACS Catal.* **2020**, *10*, 10040.
- [34] S. M. Ansar, C. L. Kitchens, *ACS Catal.* **2016**, *6*, 5553.
- [35] M. G. Mortenson, D. K. Pierce, D. A. Bryce, R. N. Wilcox, A. Lockett, M. Merzliakov, *US10980832B2* **2021**.
- [36] D. K. Pierce, M. G. Mortenson, D. A. Bryce, *US11000042B2* **2021**.
- [37] A. P. Robinson, J. Z. Zhang, H. E. Titus, M. Karl, M. Merzliakov, A. R. Dorfman, S. Karlik, M. G. Stewart, R. K. Watt, B. D. Facer, J. D. Facer, N. D. Christian, K. S. Ho, M. T. Hotchkin, M. G. Mortenson, R. H. Miller, S. D. Miller, *Sci. Rep.* **2020**, *10*, 1936.
- [38] J. Ren, R. B. Dewey III, A. Rynders, J. Evan, J. Evan, S. Ligozio, K. S. Ho, P. V. Sguigna, R. Glanzman, M. T. Hotchkin, **2023**, <https://doi.org/10.21203/rs.3.rs-3168496/v1>.
- [39] P. Sharma, P. Srivastava, A. Seth, P. N. Tripathi, A. G. Banerjee, S. K. Shrivastava, *Prog. Neurobiol.* **2019**, *174*, 53.
- [40] M. K. Jaiswal, *Med. Res. Rev.* **2019**, *39*, 733.
- [41] N. Callizot, M. Combes, A. Henriques, P. Poindron, *PLoS. One* **2019**, *14*, e0215277.
- [42] T. R. Suk, M. W. C. Rousseaux, *Mol. Neurodegener* **2020**, *15*, 45.
- [43] P. T. Nelson, D. W. Dickson, J. Q. Trojanowski, C. R. Jack, P. A. Boyle, K. Arfanakis, R. Rademakers, I. Alafuzoff, J. Attems, C. Brayne, I. T. S. Coyle-Gilchrist, H. C. Chui, D. W. Fardo, M. E. Flanagan, G. Halliday, S. R. K. Hokkanen, S. Hunter, G. A. Jicha, Y. Katsumata, C. H. Kawas, C. D. Keene, G. G. Kovacs, W. A. Kukull, A. I. Levey, N. Makkinejad, T. J. Montine, S. Murayama, M. E. Murray, S. Nag, R. A. Rissman, et al., *Brain* **2019**, *142*, 1503.
- [44] M. Combes, P. Poindron, N. Callizot, *J. Neurosci. Res.* **2015**, *93*, 633.
- [45] A. Hamelin, *J. Electroanal. Chem.* **1996**, *407*, 1.
- [46] A. Hamelin, A. M. Martins, *J. Electroanal. Chem.* **1996**, *407*, 13.
- [47] J. Zhang, M. R. Langille, M. L. Personick, K. Zhang, S. Li, C. A. Mirkin, *J. Am. Chem. Soc.* **2010**, *132*, 14012.
- [48] G. G. Li, E. Villarreal, Q. Zhang, T. Zheng, J.-J. Zhu, H. Wang, *ACS Appl. Mater. Interfaces* **2016**, *8*, 23920.
- [49] S. Pediredy, H. K. Lee, W. W. Tjiu, I. Y. Phang, H. R. Tan, S. Q. Chua, C. Troadec, X. Y. Ling, *Nat. Commun.* **2014**, *5*, 4947.
- [50] G. G. Li, Y. Lin, H. Wang, *Nano Lett.* **2016**, *16*, 7248.
- [51] S. Trasatti, O. A. Petrii, *J. Electroanal. Chem.* **1992**, *327*, 353.
- [52] P. Fischer, J. Fleckenstein, J. Hönes, *Photochem. Photobiol.* **1988**, *47*, 193.
- [53] L. D. Burke, P. F. Nugent, *Gold Bull.* **1997**, *30*, 43.
- [54] E. Villarreal, G. G. Li, Q. Zhang, X. Fu, H. Wang, *Nano. Lett.* **2017**, *17*, 4443.
- [55] Q. Zhang, D. A. Blom, H. Wang, *Chem. Mater.* **2014**, *26*, 5131.
- [56] Q. Zhang, N. Large, P. Nordlander, H. Wang, *J. Phys. Chem. Lett.* **2014**, *5*, 370.
- [57] Y. Zhang, E. Villarreal, G. G. Li, W. Wang, H. Wang, *J. Phys. Chem. Lett.* **2020**, *11*, 9321.
- [58] S. Vucic, P. Menon, W. Huynh, C. Mahoney, K. S. Ho, A. Hartford, A. Rynders, J. Evan, J. Evan, S. Ligozio, R. Glanzman, M. T. Hotchkin, M. C. Kiernan, *EClinicalMedicine* **2023**, *60*, 102036.
- [59] A. Gellé, T. Jin, L. De La Garza, G. D. Price, L. V. Besteiro, A. Moores, *Chem. Rev.* **2020**, *120*, 986.
- [60] P. Christopher, M. Moskovits, *Annu. Rev. Phys. Chem.* **2017**, *68*, 379.
- [61] J. Y. Park, S. M. Kim, H. Lee, I. I. Nedrygailov, Nedrygailov II, *Acc. Chem. Res.* **2015**, *48*, 2475.
- [62] M. L. Brongersma, N. J. Halas, P. Nordlander, *Nat. Nanotechnol.* **2015**, *10*, 25.
- [63] H. B. Tang, C. J. Chen, Z. L. Huang, J. Bright, G. W. Meng, R. S. Liu, N. Q. Wu, *J. Chem. Phys.* **2020**, *152*, 220901.
- [64] M. J. Kale, T. Avanesian, P. Christopher, *ACS Catal.* **2014**, *4*, 116.
- [65] S. Linic, U. Aslam, C. Boerigter, M. Morabito, *Nat. Mater.* **2015**, *14*, 567.
- [66] S. Linic, P. Christopher, D. B. Ingram, *Nat. Mater.* **2011**, *10*, 911.
- [67] I. Kherbouche, Y. Luo, N. Félidj, C. Mangeney, *Chem. Mater.* **2020**, *32*, 5442.
- [68] D. Devasia, A. Das, V. Mohan, P. K. Jain, *Annu. Rev. Phys. Chem.* **2021**, *72*, 423.
- [69] S. Li, H. Huang, L. Shao, J. Wang, *ACS. Nano* **2021**, *15*, 10759.
- [70] E. Cortés, L. V. Besteiro, A. Alabastri, A. Baldi, G. Tagliabue, A. Demetriadou, P. Narang, *ACS Nano* **2020**, *14*, 16202.
- [71] J. Li, S. K. Cushing, F. Meng, T. R. Senty, A. D. Bristow, N. Wu, *Nat. Photonics* **2015**, *9*, 601.
- [72] E. Kazuma, Y. Kim, *Angew. Chem., Int. Ed.* **2019**, *58*, 4800.
- [73] X. Fu, G. G. Li, E. Villarreal, H. Wang, *Nanoscale* **2019**, *11*, 7324.
- [74] J. Zhao, S. C. Nguyen, R. Ye, B. Ye, H. Weller, G. A. Somorjai, A. P. Alivisatos, F. D. Toste, *ACS Cent. Sci.* **2017**, *3*, 482.
- [75] A. O. Govorov, H. Zhang, H. V. Demir, Y. K. Gun'ko, *Nano Today* **2014**, *9*, 85.

- [76] F. Wang, C. Li, H. Chen, R. Jiang, L.-D. Sun, Q. Li, J. Wang, J. C. Yu, C.-H. Yan, *J. Am. Chem. Soc.* **2013**, *135*, 5588.
- [77] P. Christopher, H. Xin, A. Marimuthu, S. Linic, *Nat. Mater.* **2012**, *11*, 1044.
- [78] S. Mukherjee, F. Libisch, N. Large, O. Neumann, L. V. Brown, J. Cheng, J. B. Lassiter, E. A. Carter, P. Nordlander, N. J. Halas, *Nano Lett.* **2013**, *13*, 240.
- [79] D. K. Roper, W. Ahn, M. Hoepfner, *J. Phys. Chem. C* **2007**, *111*, 3636.
- [80] M. Sun, X. Fu, K. Chen, H. Wang, *ACS Appl. Mater. Interfaces* **2020**, *12*, 46146.
- [81] Z. Wang, W. Wang, M. Wamsley, D. Zhang, H. Wang, *ACS Appl. Mater. Interfaces* **2022**, *14*, 17560.
- [82] G. Gao, R. Chen, M. He, J. Li, J. Li, L. Wang, T. Sun, *Biomaterials* **2019**, *194*, 36.
- [83] T. G. De Carvalho, V. B. Garcia, A. A. De Araújo, L. H. Da Silva Gasparotto, H. Silva, G. C. B. Guerra, E. De Castro Miguel, R. F. De Carvalho Leitão, D. V. Da Silva Costa, L. J. Cruz, A. B. Chan, R. F. De Araújo Júnior, *Inter. J. Pharm.* **2018**, *548*, 1.
- [84] R. Han, L. W. C. Ho, Q. Bai, C. K. W. Chan, L. K. C. Lee, P. C.-L. Choi, C. H. J. Choi, *Nano Lett.* **2021**, *21*, 8723.
- [85] Y. Zheng, X. Zhong, Z. Li, Y. Xia, *Part. Part. Syst. Charact.* **2014**, *31*, 266.